

Article

High-Temperature Vibrational Analysis of the Lithium Mica: $2M_2$ Lepidolite

Ziyu Zhang¹, Hang Cheng^{1,2}, Li Zhang^{1,*} , Xiaoguang Li³, Xiaofeng Lu^{1,2}, Haoxiong He^{1,2}, Zhuoran Zhang¹ and Tianze Chen¹

¹ School of Earth Sciences and Resources, China University of Geosciences, Beijing 100083, China

² Center for High Pressure Science and Technology Advanced Research, Beijing 100193, China

³ State Key Laboratory of Lithospheric Evolution, Institute of Geology and Geophysics, Chinese Academy of Sciences, Beijing 100029, China

* Correspondence: li.z.zhang@cugb.edu.cn

Abstract: Lepidolite is widespread in the upper crust and can be used as a lithium ore. In the present study, in-situ high-temperature Raman and infrared spectroscopic measurements of natural Rb/Cs-free $2M_2$ lepidolite in pegmatite were conducted up to 700 °C for investigating the thermal response of lepidolite. In addition, single-crystal X-ray diffraction and electron microprobe analyses were also conducted to determine the polytype and composition of the lepidolite sample. The results show that (1) in the temperature range from 25 to 700 °C, the crystal structure of $2M_2$ lepidolite is not expected to undergo remarkable transformations upon heating and cooling; (2) the stabilities of hydroxyls in high-charge environments are lower than those in low-charge environments at elevated temperatures up to 700 °C. As a result, hydrogen ions in $2M_2$ lepidolite can transfer from the non-silicate oxygens in high-charge environments to those in low-charge environments during heating; (3) the transfers of the hydrogen ions between non-silicate oxygens in high-charge and low-charge environments may lead to the dehydration of lepidolite. Thus, lepidolites in subduction zones at temperatures below 700 °C can be sufficient to trigger partial melting and result in the release of lithium in subducted oceanic and continental slabs during subduction and exhumation.



Citation: Zhang, Z.; Cheng, H.; Zhang, L.; Li, X.; Lu, X.; He, H.; Zhang, Z.; Chen, T. High-Temperature Vibrational Analysis of the Lithium Mica: $2M_2$ Lepidolite. *Minerals* **2023**, *13*, 1112. <https://doi.org/10.3390/min13091112>

Academic Editors: Gligor Jovanovski and Petre Makreski

Received: 24 July 2023

Revised: 16 August 2023

Accepted: 17 August 2023

Published: 22 August 2023



Copyright: © 2023 by the authors. Licensee MDPI, Basel, Switzerland. This article is an open access article distributed under the terms and conditions of the Creative Commons Attribution (CC BY) license (<https://creativecommons.org/licenses/by/4.0/>).

Keywords: lepidolite; trioctahedral mica; high-temperature Raman spectroscopy; high-temperature infrared spectroscopy; hydroxyl

1. Introduction

Lithium mica generally occurs in rare-metal granites, pegmatites, and metasomatic rocks. It acquires specific chemical compositions, crystal structures, and physical properties in different forming environments. According to the composition, lithium micas are commonly divided into three main categories: Fe-poor lithium-aluminum (lepidolite, polyolithionite), ferrous lithium (zinnwaldite, protolithionite), and lithium-magnesium (taeniolite, spodiophyllite) [1–3]. As a typical Fe-poor lithium mica, lepidolite (ideal formula $KLi_{1.5}Al_{1.5}AlSi_3O_{10}F_2$) is widespread in the upper crust and can be used as a lithium ore. Natural lepidolite is generally formed via the replacement of muscovite or biotite, or through the reaction among other Li-bearing silicates, K-feldspar, and F-rich fluids. It has a complex chemical composition that varies between trilithionite ($KLi_{1.5}Al_{1.5}AlSi_3O_{10}F_2$) and polyolithionite ($KLi_2AlSi_4O_{10}F_2$). In addition, it is also considered as a potential source of rubidium and cesium, since a variety of lepidolite is usually enriched in these important rare metals [4–8].

Lepidolite has a tetrahedral-octahedral-tetrahedral (T-O-T) layered structure where the tri-octahedral layer is located between two tetrahedral sheets. The interlaminar spaces are normally filled with K^+ cation. Based on different octahedral ordering schemes, it crystallizes in several polytypes [9–11]. The $3T$ polytype (space group $P3_112$) contains two large

octahedral sites (M1 and M2) that are occupied by lithium ion and a small aluminum-rich octahedral site (M3). In contrast, the 1M (space group $C2/m$), $2M_1$ (space group $C2/c$), and $2M_2$ (space group $C2/c$) (Figure 1) polytypes have only one large octahedral site (M1) that contains lithium ion and two small symmetry-related octahedral sites (M2) that can be occupied by both lithium and aluminum cations. In all polytypes, the non-silicate oxygen site is the potential position for protonation (such as O3 in the lepidolite- $2M_2$ structure) [10,12].

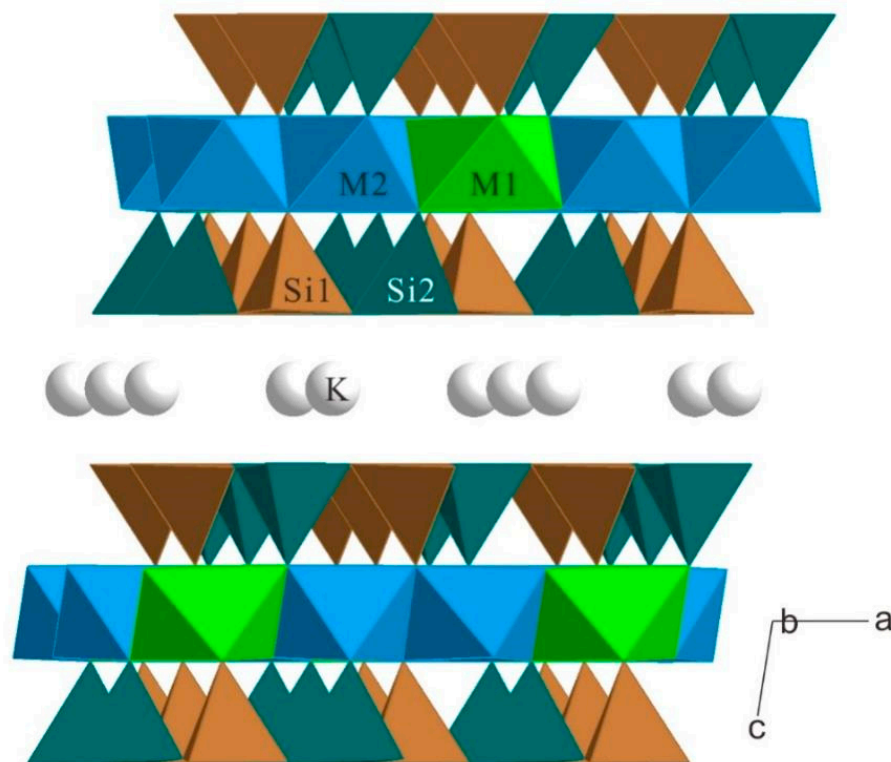


Figure 1. Projection of crystal structure of $2M_2$ lepidolite modified after [10]. M1 and M2 represent two symmetrically distinct octahedral sites; Si1 and Si2 represent two symmetrically distinct tetrahedral sites; K represents interlamellar cation. a, b, and c represent three axes.

Natural lepidolite commonly has a high fluorine content. Therefore, experimental data related to the hydroxyl groups in its crystal structure is relatively limited [13]. Robert et al. (1989) [13] identified the octahedrally coordinated cations bonded to different types of hydroxyl and investigated the factors that affect the features of O-H bands in the infrared and Raman spectra of synthetic lepidolites. The observations in their study indicated that the wavenumbers of OH-stretching bands are determined by bond-valence sum received by hydroxyl oxygen from its three adjacent cations. In addition, the wavenumber gap among different OH-stretching band-types increases with increasing aluminum ($^{VI}Al + ^{IV}Al$) contents of lepidolite.

In subduction zones, mica is a significant mineral host for fluid-mobile elements and it dictates the recycling behavior of lithium in the crust and mantle. The devolatilization of lithium-rich mica may generate the partial melting and drive the lithium release of the subducted slabs [14]. The aim of the present work is to reveal the thermal response of lepidolite and the stability of hydroxyl ion in the crystal structure of lepidolite at elevated temperatures. Thus, in-situ high-temperature Raman and infrared spectroscopic measurements of a natural Rb/Cs-free lepidolite sample were conducted up to 700 °C. Single-crystal X-ray diffraction and electron microprobe analyses were also conducted to determine the polytype and chemical composition of the lepidolite sample.

2. Experimental Methods

The lepidolite sample in pegmatite dyke was collected from the Koktokay area in Altay. A photograph of the sample is shown in Figure 2. The chemical composition of lepidolite was measured via a JEOL JXA-8230 electron probe microanalyzer in Testing Center of Shandong Bureau of China Metallurgical Geology Bureau, at an accelerating voltage of 15 kV, a beam current of 20 nA, and a beam size of 1 μm . Mineral and metal standards were used: Aluminum (Al), Fluorite (F), Jadeite (Na, Si), and Sanidine (K).



Figure 2. Photograph of lepidolite sample from the pegmatite dyke in Koktokay area.

Single crystal of natural lepidolite (about $60 \times 40 \times 20 \mu\text{m}$ in size) was mounted on glass fiber for single-crystal X-ray diffraction analysis. Intensity data were collected with a Bruker D8 Venture diffractometer equipped with a four-circle goniometer and a CCD detector at Center for High Pressure Science and Technology Advanced Research, Beijing. X-ray ($\lambda = 0.71073 \text{ \AA}$) was generated using a rotating Mo anode of $\mu\text{S 3.0}$ generator. The collection strategy was optimized with the APEX4 software. The crystal structure of lepidolite was refined from the intensity data via SHELXL-2018 [15] in the package WINGX [16], based on the previously reported scattering factors and absorption coefficients from the International Tables for Crystallography, Volume C [17].

Raman spectra of a lepidolite flake (about $200 \times 150 \times 50 \mu\text{m}$ in size) were collected at 25, 100, 200, 300, 400, 500, 600, and 700 $^{\circ}\text{C}$ during heating and cooling, using a WITec's confocal Raman imaging microscope alpha300 R at the Institute of Geology and Geophysics, Chinese Academy of Sciences. A Linkam TS1400 heating stage equipped with a SiO_2 window and a Rh/Pt thermocouple was used for in-situ high-temperature measurements. The spectra were excited by a 488-nm solid-state laser at a power of 50 mW. A $20\times$ objective was employed to focus the incident laser and collect the scattered light. All spectra were collected in the wavenumber range from 100 to 4000 cm^{-1} , using 15 accumulations with 20 s exposure time. Increasing and decreasing rates of temperature were 100 $^{\circ}\text{C}/\text{min}$ and $-100 \text{ }^{\circ}\text{C}/\text{min}$, respectively. The sample was held at each temperature for at least 10 min to reach equilibrium during data collection.

Unpolarized infrared absorption spectra of a lepidolite chip (about $100 \times 70 \times 50 \mu\text{m}$ in size) were collected at 25, 100, 200, 300, 400, 500, 600, and 700 $^{\circ}\text{C}$ during heating and cool-

ing, using a Bruker INVENIO-R FTIR spectrometer with a 20× objective on the HYPERION 1000 microscope at Institute of Geology and Geophysics, Chinese Academy of Sciences. A Linkam TS1400 heating stage equipped with a SiO₂ window and a Rh/Pt thermocouple was also employed. Each spectrum was collected in the range from 3000 to 3800 cm⁻¹ with a resolution of 2 cm⁻¹ and accumulated over 128 scans. Increasing and decreasing rates of temperature were set at 100 °C/min and −100 °C/min, respectively. During data collection, the sample was held at each temperature for over 10 min to reach equilibrium.

3. Result and Discussion

The unit-cell determination of the single-crystal X-ray diffraction analysis indicates that the lepidolite sample in this study belongs to 2M₂ polytype (space group C2/c). The refined unit-cell parameters are $a = 9.014(6)$ Å, $b = 5.202(4)$ Å, $c = 20.223(14)$ Å, $\beta = 99.330(17)^\circ$. The estimated atom positions and polyhedral volumes are given in Table 1. Previous studies of mica group minerals from a variety of geological localities showed that natural micas (include certain lithium-rich mica samples) commonly have a stacking-disordered structure or present a complex layer-stacking sequence [18,19]. In this case, the accuracy of the crystal structure refinement (R_{int} , R_{sigma} , R_1 and $GooF$ are 0.1152, 0.0514, 0.0615 and 1.001 respectively) can be limited.

Table 1. Unit-cell, atom position, and polyhedral volume parameters for lepidolite (2M₂).

<i>a</i>	<i>b</i>	<i>c</i>	β	Volume ^a	Space Group	
9.014(6)	5.202(4)	20.223(14)	99.3302	935.59	C2/c	
□	M2 (Al/Li)	K	M1 (Li)	Si1 (Si/Al)	Si2 (Si/Al)	□
X	0.579(3)	0.5	0.25	0.790(4)	0.131(5)	
Y	0.220(11)	0.422(6)	0.25	0.417(10)	0.405(7)	
Z	0	0.25	0	0.130(1)	0.135(3)	
Volume ^b	10.203	–	12.118	2.254	2.147	
□	O1	O2	O3(F)	O4	O5	O6
X	0.770(5)	0.100(5)	0.442(5)	0.702(8)	0.254(9)	0.975(8)
Y	0.387(7)	0.425(8)	0.424(6)	0.179(12)	0.179	0.403(11)
Z	0.050(3)	0.059(4)	0.047(1)	0.168(5)	0.164(5)	0.166(3)

Notes: ^a unit-cell volume; ^b polyhedral volume.

According to electron microprobe analysis, the lepidolite sample contains 27.78 wt.% Al₂O₃, 51.10 wt.% SiO₂, 10.17 wt.% K₂O, 6.74 wt.% F, and 0.40 wt.% Na₂O. Li₂O content is calculated to be 5.11 wt.% based on the previously reported relationship (expressed in wt.% oxide): Li₂O = (0.287 × SiO₂) − 9.552 [20,21]. Thus, the formula unit of lepidolite is estimated to be K_{0.80}Na_{0.05}(Li_{1.27}Al_{1.17})(Si_{3.15}Al_{0.85})O_{10.69}F_{1.31}H_{0.63}, assuming a total sum of 100 wt.%. The estimated formula implies a tetrahedral Si/Al molar ratio of 3.70 and a Al/Li molar ratio of 2.54 at M2 site (the larger M1 site is only occupied by Li⁺).

The Raman spectrum of lepidolite collected at ambient condition (25 °C) displays five strong bands at 259(ν_{R1}), 421(ν_{R2}), 574(ν_{R4}), 708(ν_{R5}), and 753(ν_{R6}) cm⁻¹, and a weak band at 466(ν_{R3}) in the wavenumber range of 100–1200 cm⁻¹ (Figure 3 and Table 2). The band at 259 cm⁻¹ can be ascribed to OH (hydroxyl), K (potassium) and O (oxygen) translational motions [22,23]. The band at 421 cm⁻¹ is due to M-O (cation-oxygen bonds at octahedral sites) stretching motion and translations of T (cations at tetrahedral sites), M (cations at octahedral sites), and O [24]. The band at 574 cm⁻¹ is related with O, T, K and M translational motions [22]. The doublet bands at 708 and 753 cm⁻¹ are attributed to O-T-O and T-O-T bending motions, M-O stretch, and translations of oxygens [24]. Although the O-H bands (in the wavenumber range of 3000–3800 cm⁻¹) can be observed in the infrared spectra collected in this study, they can hardly be recognized in the recorded Raman spectra due to the high fluorine concentration and the low water content of the lepidolite sample.

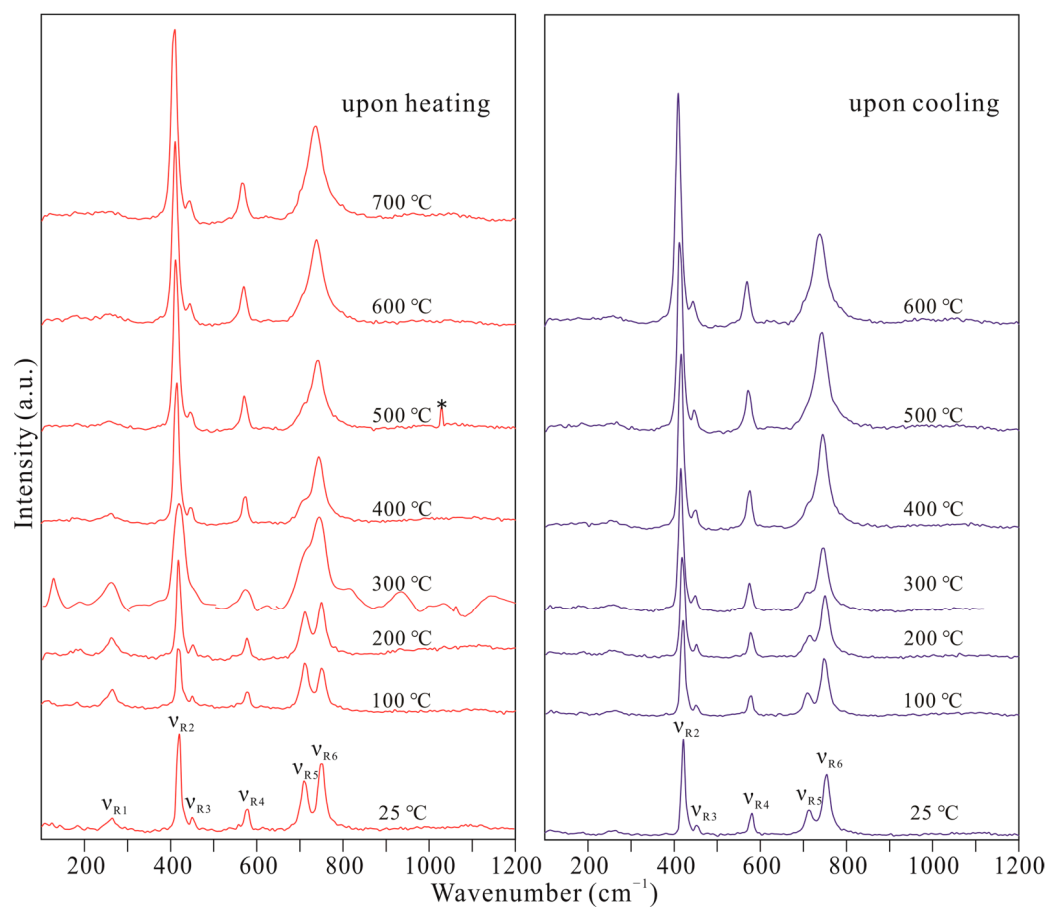


Figure 3. Raman spectra of lepidolite in the wavenumber range of 100–1200 cm^{-1} under varying temperature from 25 to 700 $^{\circ}\text{C}$. Spectra in red and blue were collected during heating and cooling, respectively. * The signal from cosmic rays.

Table 2. The band frequencies (cm^{-1}) of the spectra from in-situ high-temperature Raman spectroscopic measurements.

T ($^{\circ}\text{C}$)	Upon Heating						
	ν_{R1}	ν_{R2}	ν_{R3}	ν_{R4}	ν_{R5}	ν_{R6}	
25	259	421	466	574	708	753	
100	265	421	466	574	708	747	
200	259	415	466	574	708	747	
300	259	415	466	570	708	741	
400		415	461	568	708	742	
500		409	461	568	703	736	
600		409	455	568	697	736	
700		409	455	563		736	
T ($^{\circ}\text{C}$)	Upon cooling						
	ν_{R1}	ν_{R2}	ν_{R3}	ν_{R4}	ν_{R5}	ν_{R6}	
	600		409	455	568	697	736
	500		409	461	568	697	742
	400		415	461	574	703	742
	300		415	466	574	708	747
	200		421	466	574	708	747
100		421	466	574	708	753	
25		421	472	580	708	753	

As shown in Figure 4 and Table 2, the ν_{R2} , ν_{R3} , ν_{R4} , ν_{R5} , and ν_{R6} bands show negative shifts with an increasing temperature up to 700 °C at -0.018 , -0.016 , -0.016 , -0.018 , and -0.024 $\text{cm}^{-1}/^{\circ}\text{C}$, respectively. All these bands (ν_{R2-R6}) are fully reversible in positions upon cooling and no new bands are observed at ambient condition (25 °C) after the experiment, indicating that the crystal structure of the lepidolite sample should not have undergone remarkable transformations in the temperature range of the present study (25–700 °C). The ν_{R1} band shows a slight change in position at elevated temperatures up to 300 °C and disappears at 400 °C. In addition, two new bands at about 125 and 945 cm^{-1} occur in the Raman spectrum at 300 °C. However, they disappear with ν_{R1} at higher temperatures and are irreversible upon cooling. According to [22], these two bands are due to translational and librational motions of the tetrahedra, T-O stretching motion, and translation of K.

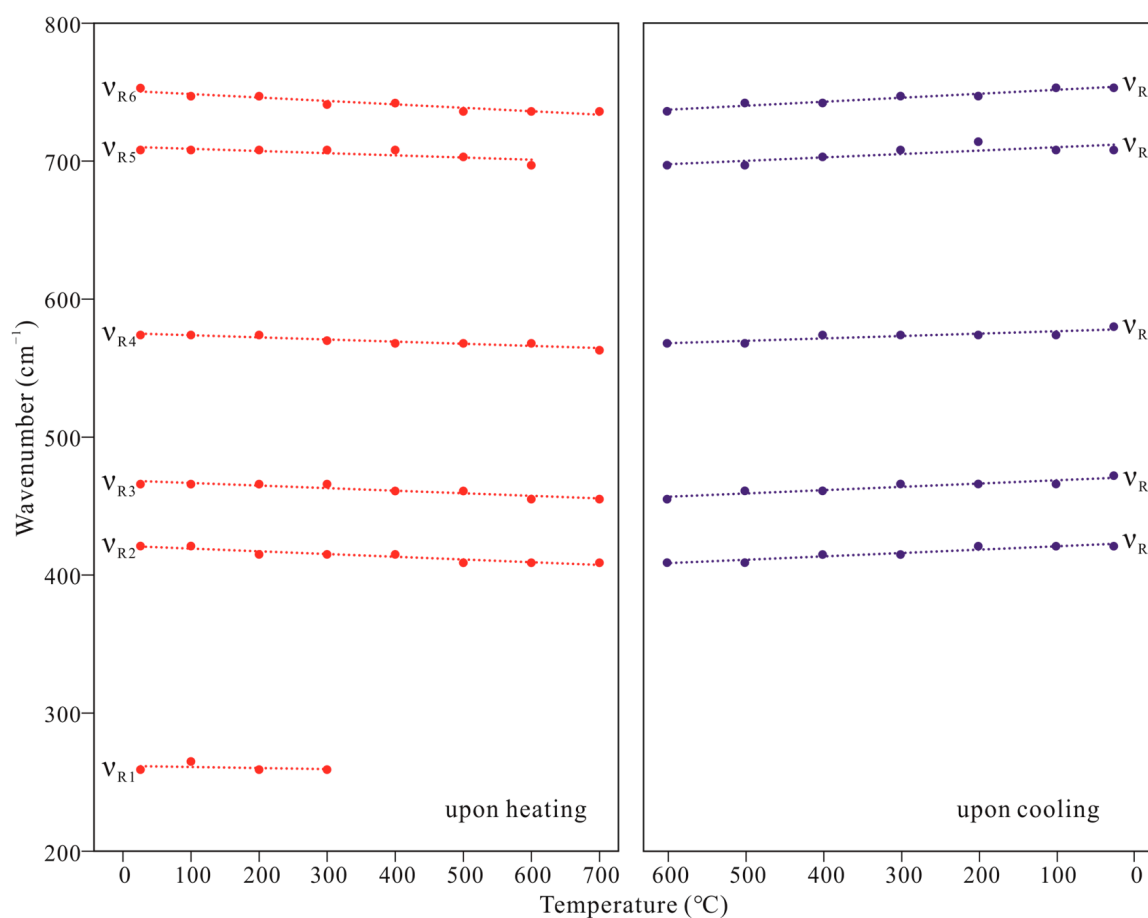


Figure 4. Variations in band wavenumbers (cm^{-1}) in the Raman spectra with varying temperatures upon heating and cooling.

At ambient condition (25 °C), the mid-infrared spectrum of lepidolite displays seven absorption bands at 3284, 3392, 3560, 3581, 3625, 3645 and 3660 cm^{-1} (Figure 5). The five intense bands at 3560, 3581, 3625, 3645 and 3660 cm^{-1} are due to hydroxyl-stretching vibrations [13,23,25,26], while the two weak bands at 3284 and 3392 cm^{-1} are attributed to water molecules [27] and cannot be observed at elevated temperatures.

Robert et al. (1989) [13] indicated that the higher bond-valence sum received by the non-silicate O3 from its three adjacent cations (Al^{3+} and Li^+) at the octahedral sites, the lower the bond valence exchanged within the hydroxyl, and therefore the lower wavenumber of the O-H stretching band. According to their investigations, the five O-H bands observed at ambient condition (Figure 5) in the present study belong to TRI-7 bands, which are due to a 7-charge environment (hydroxyl bonded to Al_2Li) (Figure 6).

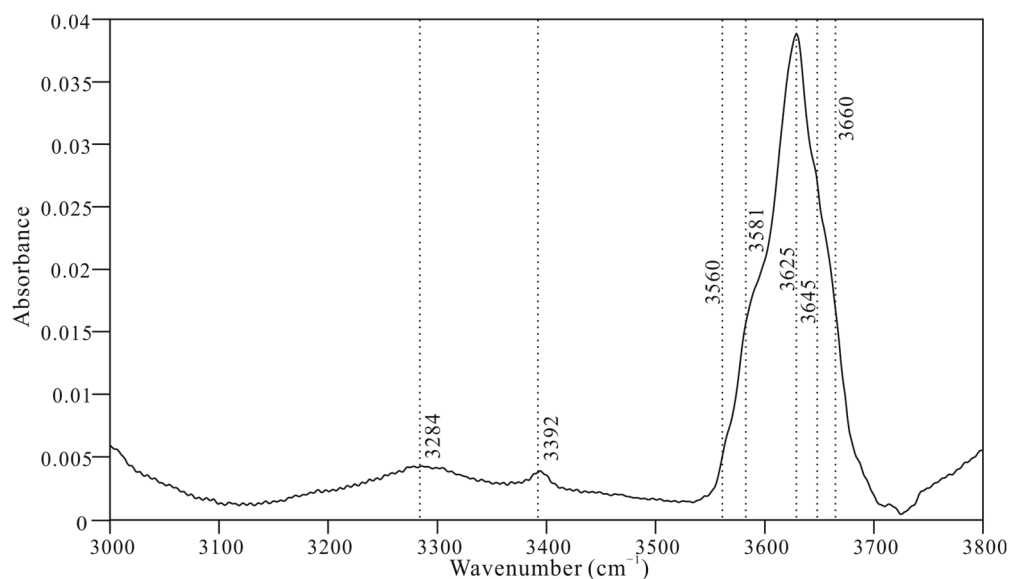


Figure 5. The infrared absorption spectrum (solid line) of lepidolite at ambient condition corresponding to O-H stretching modes in the wavenumber range from 3000 to 3800 cm^{-1} . Dashed lines indicate the wavenumbers of the bands.

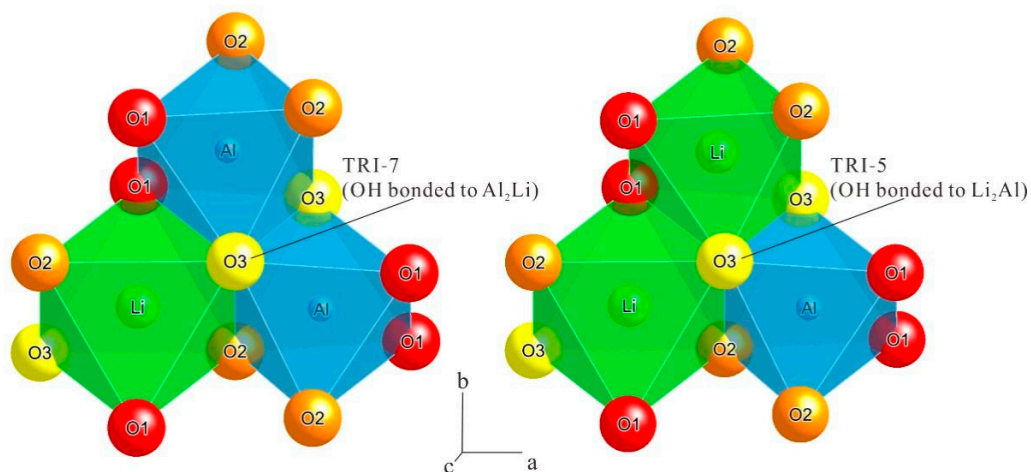


Figure 6. The two charge environments of the non-silicate O3 site (potential position for protonation) in the $2M_2$ lepidolite. The crystal structure of $2M_2$ lepidolite is modified after [10]. According to [28], cation radii of Li^+ and Al^{3+} in octahedral sites are 0.76 Å and 0.535 Å, respectively. a, b, and c represent three axes.

As shown in Figures 7 and 8, at elevated temperatures up to 400 °C, the bands at 3560 ($\nu_{\text{IR}1}$), 3581 ($\nu_{\text{IR}2}$), and 3645 ($\nu_{\text{IR}6}$) shift to higher frequencies, while the band at 3625 ($\nu_{\text{IR}3}$) exhibits a linear negative shift (Table 3). In micas, the O-H dipoles commonly lie nearly parallel to the (001) plane [29,30]. In this case, the O-H stretching bands show a positive shift upon heating, resulting from strengthening of the O-H covalent bonds and weakening of the hydrogen-bonding interactions between the hydroxyl protons and the oxygen atoms of surrounding tetrahedra [18,23,31,32]. In addition, the O-H dipoles in lepidolite can also show a higher angle of tilt [33]. As a result, the repulsion between the hydroxyl protons (H^+) and the interlayer cations (K^+ or Na^+) can be strong due to this orientation [13]. Therefore, the shifts of the $\nu_{\text{IR}1}$, $\nu_{\text{IR}2}$, and $\nu_{\text{IR}6}$ bands can be due to the thermal response of the O-H dipoles, which are nearly parallel to (001). The downshift of the $\nu_{\text{IR}3}$ band can be explained by the weakening of the repulsion between the interlayer cations and the protons that belong to the tilted O-H dipoles.

Under varying temperature from 100 to 500 °C, a number of new bands ($\nu_{\text{IR8}}\text{--}\nu_{\text{IR17}}$) at higher wavenumbers instantaneously appear in the mid-infrared spectra during heating (Table 3). According to [13], many of these O-H bands belong to TRI-5 bands, which are due to a 5-charge environment (hydroxyl bonded to Li2Al) (Figure 6). As shown in Figure 7, the intensities of these bands increase with increasing temperature up to 700 °C. In contrast, the bands at lower wavenumbers (such as TRI-7 bands) show remarkable decreases in intensity upon heating and disappear at 600 °C (Table 3), implying that hydrogen ions in $2M_2$ lepidolite can transfer from the non-silicate oxygens in high-charge environments to those in low-charge environments. During cooling, the intensities of the bands at higher wavenumbers decrease with decreasing temperature, while the bands at lower wavenumbers reappear and exhibit slight increases in intensity (Figure 7 and Table 3), indicating that the stabilities of the hydroxyls in low-charge environments are relatively low compared to those in high-charge environments at low temperatures.

As shown in Figure 7, at ambient condition, the O-H bands in the spectrum after cooling are significantly weaker than those before heating, revealing that the transfers of the hydrogen ions between non-silicate oxygens in high-charge and low-charge environments during heating and cooling may contribute to the dehydration of lepidolite. Therefore, in subduction zones, lepidolites can be sufficient to trigger original partial melting of the slabs and the release of lithium at temperature below 700 °C during subduction and exhumation.

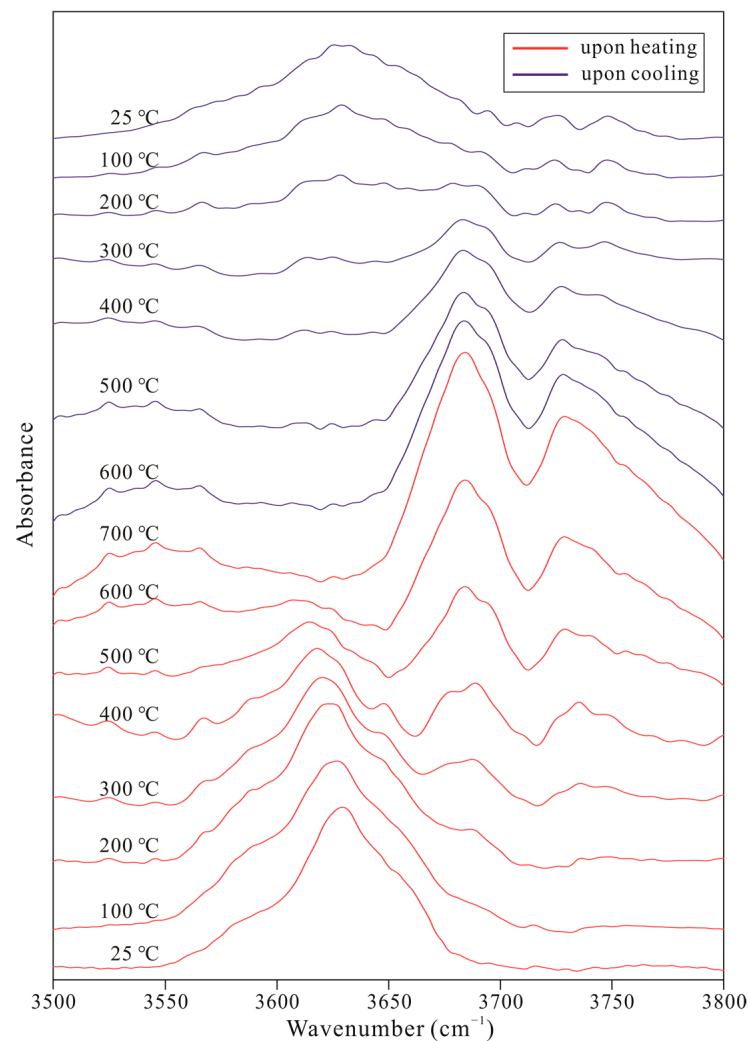


Figure 7. Mid-infrared spectra of lepidolite in the wavenumber range from 3500 to 3800 cm^{-1} under varying temperature from 25 to 700 °C. Spectra in red and blue were collected during heating and cooling, respectively.

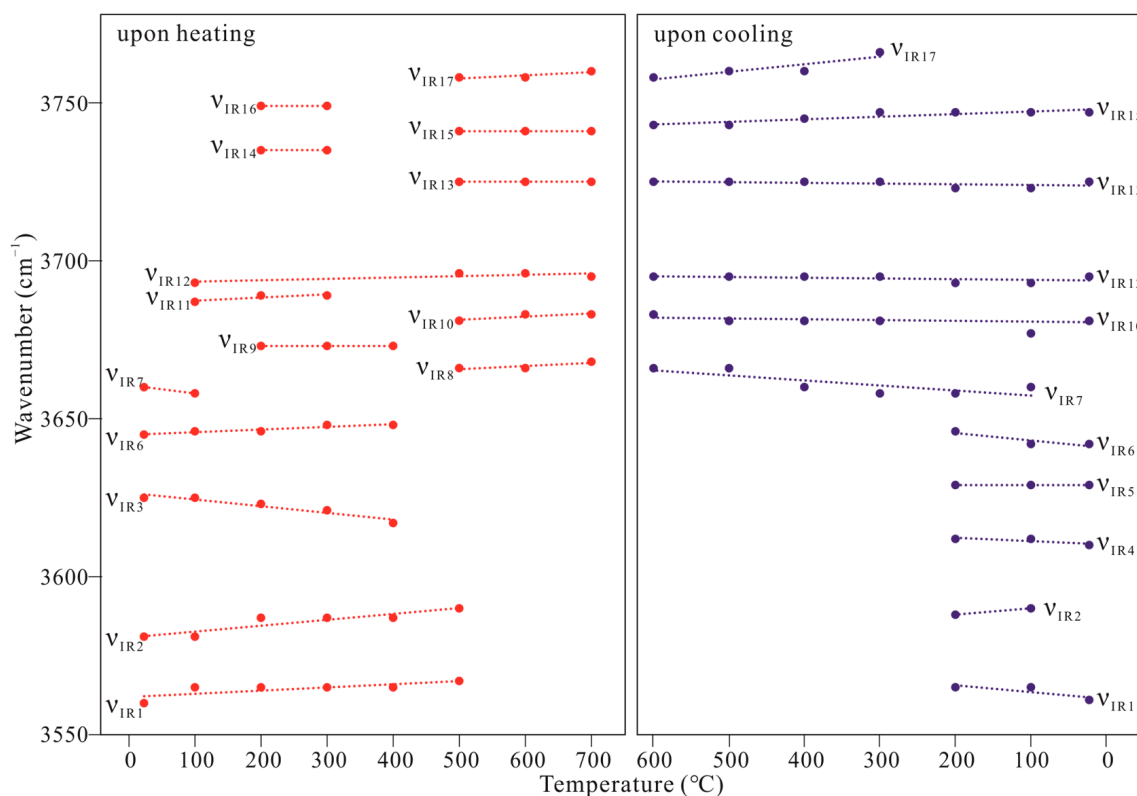


Figure 8. Variations in band wavenumbers (cm^{-1}) in the mid-infrared spectra with varying temperatures upon heating and cooling.

Table 3. The band frequencies (cm^{-1}) of the spectra from in-situ high-temperature FTIR spectroscopic measurements.

T(°C)	Upon Heating																
	ν_{IR1}	ν_{IR2}	ν_{IR3}	ν_{IR4}	ν_{IR5}	ν_{IR6}	ν_{IR7}	ν_{IR8}	ν_{IR9}	ν_{IR10}	ν_{IR11}	ν_{IR12}	ν_{IR13}	ν_{IR14}	ν_{IR15}	ν_{IR16}	ν_{IR17}
25	3560	3581	3625	—	—	3645	3660	—	—	—	—	—	—	—	—	—	—
100	3565	3581	3625	—	—	3646	3658	—	—	—	3687	3693	—	—	—	—	—
200	3565	3587	3623	—	—	3646	—	—	3673	—	3689	—	—	3735	—	3749	—
300	3565	3587	3621	—	—	3648	—	—	3673	—	3689	—	—	3735	—	3749	—
400	3565	3587	3617	—	—	3648	—	—	3673	—	—	—	—	—	—	—	—
500	3567	3590	—	—	—	—	—	3666	—	3681	—	3696	3725	—	3741	—	3758
600	—	—	—	—	—	—	—	3666	—	3683	—	3696	3725	—	3741	—	3758
700	—	—	—	—	—	—	—	3668	—	3683	—	3695	3725	—	3741	—	3760
T (°C)	Upon cooling																
	ν_{IR1}	ν_{IR2}	ν_{IR3}	ν_{IR4}	ν_{IR5}	ν_{IR6}	ν_{IR7}	ν_{IR8}	ν_{IR9}	ν_{IR10}	ν_{IR11}	ν_{IR12}	ν_{IR13}	ν_{IR14}	ν_{IR15}	ν_{IR16}	ν_{IR17}
600	—	—	—	—	—	—	3666	—	—	3683	—	3695	3725	—	3743	—	3758
500	—	—	—	—	—	—	3666	—	—	3681	—	3695	3725	—	3743	—	3760
400	—	—	—	—	—	—	3660	—	—	3681	—	3695	3725	—	3745	—	3760
300	—	—	—	—	—	—	3658	—	—	3681	—	3695	3725	—	3747	—	3766
200	3565	3588	—	3612	3629	3646	3658	—	—	—	—	3693	3723	—	3747	—	—
100	3565	3590	—	3612	3629	3642	3660	—	—	3677	—	3693	3723	—	3747	—	—
25	3561	—	—	3610	3629	3642	—	—	—	3681	—	3695	3725	—	3747	—	—

4. Conclusions

High-temperature Raman spectroscopy indicates that the crystal structure of $2M_2$ lepidolite is not expected to undergo remarkable transformations in the temperature range from 25 to 700 °C upon heating and cooling.

Hydrogen ions in $2M_2$ lepidolite can transfer from the non-silicate oxygens in high-charge environments to those in low-charge environments in the temperature range from 100 to 700 °C upon heating, implying that the stabilities of hydroxyls in high-charge environments are lower than those in low-charge environments at high temperatures.

The transfers of the hydrogen ions between non-silicate oxygens in high-charge and low-charge environments under varying temperature from 25 to 700 °C may result in the dehydration of lepidolite. Therefore, as an important reservoir for lithium in subduction zones, lepidolite is expected to trigger partial melting and lithium release of subducted slabs during subduction and exhumation at temperatures below 700 °C.

Author Contributions: L.Z. suggested the basis of the paper; Z.Z. (Ziyu Zhang) and L.Z. wrote the paper; Z.Z. (Ziyu Zhang) and X.L. (Xiaofeng Lu) performed high-temperature Raman spectroscopic measurements; Z.Z. (Ziyu Zhang) and X.L. (Xiaoguang Li) performed high-temperature infrared spectroscopic measurements. Z.Z. (Ziyu Zhang) and H.C. performed electron microprobe analysis; L.Z. and Z.Z. (Zhuoran Zhang) performed single-crystal X-ray diffraction analysis; H.H. and T.C. discussed the methods and results. All authors have read and agreed to the published version of the manuscript.

Funding: This study was supported by the National Natural Science Foundation of China (no. 42172044).

Data Availability Statement: Not applicable.

Conflicts of Interest: The authors declare no conflict of interest.

References

1. Grew, E.S.; Bosi, F.; Ros, L.; Kristiansson, P.; Gunter, M.E.; Halenius, U.; Trumbull, R.B.; Yates, M. Fluor-elbaite, lepidolite and Ta-Nb oxides from a pegmatite of the 3000 Ma Sinceni Pluton, Swaziland: Evidence for lithium-cesium-tantalum (LCT) pegmatites in the Mesoarchean. *Eur. J. Miner.* **2018**, *30*, 205–218. [[CrossRef](#)]
2. Ogorodova, L.P.; Kiseleva, I.A.; Melchakova, L.V. Thermodynamic properties of lithium micas. *Geochem. Int.* **2010**, *48*, 415–418. [[CrossRef](#)]
3. Roda, E.; Keller, P.; Pesquera, A.; Fontan, F. Micas of the muscovite-lepidolite series from Karibib pegmatites, Namibia. *Miner. Mag.* **2007**, *71*, 41–62. [[CrossRef](#)]
4. Lv, Y.; Ma, B.; Liu, Y.; Wang, C.; Zhang, W.; Chen, Y. Selective extraction of cesium from high concentration rubidium chloride leach liquor of lepidolite. *Desalination* **2022**, *530*, 115673. [[CrossRef](#)]
5. Munoz, J.L. Physical properties of synthetic lepidolites. *Am. Miner.* **1968**, *53*, 1490–1512.
6. Ogorodova, L.P.; Kiseleva, I.A.; Melchakova, L.V.; Schuriga, T.N. Thermodynamic properties of lithium mica: Lepidolite. *Thermochim. Acta* **2005**, *43*, 68–70. [[CrossRef](#)]
7. Paukov, I.E.; Kovalevskaya, Y.A.; Kiseleva, I.A.; Schuriga, T.N. Thermodynamic properties of natural lepidolite. *Geochem. Int.* **2007**, *45*, 559–563. [[CrossRef](#)]
8. Zhang, X.; Chen, Z.; Rohani, S.; He, M.; Tan, X.; Liu, W. Simultaneous extraction of lithium, rubidium, cesium and potassium from lepidolite via roasting with iron(II) sulfate followed by water leaching. *Hydrometallurgy* **2022**, *208*, 105820. [[CrossRef](#)]
9. Brown, B.E. The crystal structure of a $3T$ lepidolite. *Am. Miner.* **1978**, *63*, 332–336.
10. Guggenheim, S. Cation ordering in lepidolite. *Am. Miner.* **1981**, *66*, 1221–1232.
11. Swanson, T.H.; Bailey, S.W. Redetermination of the lepidolite- $2M_1$ structure. *Clay Clay Miner.* **1981**, *29*, 81–90. [[CrossRef](#)]
12. Sartori, F.; Franzini, M.; Merlino, S. Crystal structure of a $2M_2$ lepidolite. *Acta Crystallogr. B* **1973**, *29*, 573–578. [[CrossRef](#)]
13. Robert, J.; Beny, J.; Beny, C.; Volfinger, M. Characterization of lepidolites by Raman and infrared spectrometries. I. Relationships between OH-stretching wavenumbers and composition. *Can. Miner.* **1989**, *27*, 225–235.
14. Bebout, G.E.; Bebout, A.E.; Graham, C.M. Cycling of B, Li, and LILE (K, Cs, Rb, Ba, Sr) into subduction zones: SIMS evidence from micas in high-P/T metasedimentary rocks. *Chem. Geol.* **2007**, *239*, 284–304. [[CrossRef](#)]
15. Sheldrick, G.M. *SHELXL: Programs for Crystal Structure Analysis*; University of Göttingen: Göttingen, Germany, 2018.
16. Farrugia, L.J. WinGX suite for small-molecule single-crystal crystallography. *J. Appl. Crystallogr.* **1999**, *32*, 837–838. [[CrossRef](#)]
17. Prince, E. Volume C: Mathematical Physical and Chemical Tables. In *International Tables for Crystallography*, 3rd ed.; Reidel: Dordrecht, The Netherlands, 2004.
18. He, X.; Zhang, L.; Kagi, H.; Smyth, J.R.; Komatsu, K.; Li, X.; Gao, J.; Lei, L. In-Situ high-pressure and high-temperature spectroscopic studies of phengite in ultrahigh-pressure eclogite: Implications for water transport during ultra-deep continental subduction. *Phys. Chem. Miner.* **2022**, *49*, 24. [[CrossRef](#)]
19. Ross, M.; Takeda, H.; Wones, D.R. Mica polytypes: Systematic description and identification. *Science* **1966**, *151*, 191–193. [[CrossRef](#)]
20. Tindle, A.G.; Webb, P.C. Estimation of lithium contents in trioctahedral micas using microprobe data: Application to micas from granitic rocks. *Eur. J. Miner.* **1990**, *2*, 595–610. [[CrossRef](#)]
21. Tian, R.; Zhang, H.; Lyu, Z.; Tang, Y. Mineralogical characteristics of micas in the Xiaohusite No. 91 pegmatite dyke in the Koktokay area, Xinjiang and their geological significances. *Acta Miner. Sin.* **2021**, *41*, 593–609.

22. McKeown, D.A.; Bell, M.I.; Etz, E.S. Vibrational analysis of the dioctahedral mica: $2M_1$ muscovite. *Am. Miner.* **1999**, *84*, 1041–1048. [[CrossRef](#)]
23. Williams, Q.; Knittle, E.; Scott, H.P.; Liu, Z.X. The high-pressure behavior of micas: Vibrational spectra of muscovite, biotite, and phlogopite to 30 GPa. *Am. Miner.* **2012**, *97*, 241–252. [[CrossRef](#)]
24. Goryainov, S.V.; Krylov, A.S.; Polyansky, O.P.; Vtyurin, A.N. In-situ Raman study of phengite compressed in water medium under simultaneously high P – T parameters. *J. Raman Spectrosc.* **2017**, *48*, 1431–1437. [[CrossRef](#)]
25. Wang, Y.; Yuan, X.; Fu, H. Mineralogical characteristics of gem-quality lepidolite rock in Xinjiang. *J. Gem Gemmol.* **2014**, *16*, 22–28.
26. Huang, W.H.; Yang, Y.; Qi, Z.M.; Liu, W.D.; Wang, Z.P.; Liu, Y.; Xia, Q.K. Ammonium impacts on vibrations of hydroxyl and lattice of phengite at high temperature and high pressure. *J. Earth Sci.* **2021**, *32*, 1278–1286. [[CrossRef](#)]
27. Johnson, E.A. Water in nominally anhydrous crustal minerals: Speciation, concentration, and geologic significance. *Rev. Mineral. Geochem.* **2006**, *62*, 117–154. [[CrossRef](#)]
28. Shannon, R.D. Revised effective ionic-radii and systematic studies of interatomic distances in halides and chalcogenides. *Acta Crystallogr. A* **1976**, *32*, 751–767. [[CrossRef](#)]
29. Pavese, A.; Ferraris, G.; Prencipe, M.; Ibberson, R. Cation site ordering in phengite 3T from the Dora-Maira massif (western Alps): A variable-temperature neutron powder diffraction study. *Eur. J. Miner.* **1997**, *9*, 1183–1190. [[CrossRef](#)]
30. Pavese, A.; Ferraris, G.; Pischedda, V.; Ibberson, R. Tetrahedral order in phengite $2M_1$ upon heating, from powder neutron diffraction, and thermodynamic consequences. *Eur. J. Miner.* **1999**, *11*, 309–320. [[CrossRef](#)]
31. Libowitzky, E. Correlation of O–H stretching frequencies and O–H···O hydrogen bond lengths in minerals. *Monatsh. Chem.* **1999**, *130*, 1047–1059. [[CrossRef](#)]
32. Robert, J.L.; Kodama, H. Generalization of the correlations between hydroxyl-stretching wavenumbers and composition of micas in the system K_2O – MgO – Al_2O_3 – SiO_2 – H_2O : A single model for trioctahedral and dioctahedral micas. *Am. J. Sci.* **1988**, *288*, 196–212.
33. Lin, J.C.; Guggenheim, S. The crystal structure of a Li, Be-rich brittle mica: A dioctahedral-trioctahedral intermediate. *Am. Miner.* **1983**, *68*, 130–142.

Disclaimer/Publisher’s Note: The statements, opinions and data contained in all publications are solely those of the individual author(s) and contributor(s) and not of MDPI and/or the editor(s). MDPI and/or the editor(s) disclaim responsibility for any injury to people or property resulting from any ideas, methods, instructions or products referred to in the content.